Cooperative Enhancement of Second-Harmonic Generation from a Single CdS Nanobelt-Hybrid Plasmonic Structure

Xinfeng Liu,[†] Qing Zhang,[†] Wee Kiang Chong,[†] Jing Ngei Yip,[†] Xinglin Wen,[†] Zhenpeng Li,[†] Fengxia Wei,[‡] Guannan Yu,[†] Qihua Xiong,[*,†,§] and Tze Chien Sum[*,†,‡]

[†]Division of Physics and Applied Physics, School of Physical and Mathematical Sciences, Nanyang Technological University, Singapore 637371, [‡]Energy Research Institute@NTU (ERI@N), Nanyang Technological University, 50 Nanyang Drive, Singapore 637553, and [§]NOVITAS, Nanoelectronics Center of Excellence, School of Electrical and Electronic Engineering, Nanyang Technological University, Singapore 639798

ABSTRACT Semiconductor nanostructures (*e.g.*, nanowires and nanobelts) hold great promise as subwavelength coherent light sources, nonlinear optical frequency converters, and all-optical signal processors for optoelectronic applications. However, at such small scales, optical second-harmonic generation (SHG) is generally inefficient. Herein, we report on a straightforward strategy using a thin Au layer to enhance the SHG from a single CdS nanobelt by 3 orders of magnitude. Through detailed experimental and theoretical analysis, we validate that the augmented SHG originates from the mutual intensification of the local fields induced by the plasmonic nanocavity and by the reflections within the CdS Fabry–Pérot resonant cavity in this hybrid semiconductor–metal system. Polarization-dependent SHG measurements can be employed to determine and distinguish the contributions of SH signals from the CdS nanobelt and gold film, respectively. When the thickness of gold film becomes comparable to the skin depth, SHG from the gold film can be clearly observed. Our work demonstrates a facile approach for tuning the nonlinear optical properties of mesoscopic, nanostructured, and layered semiconductor materials.

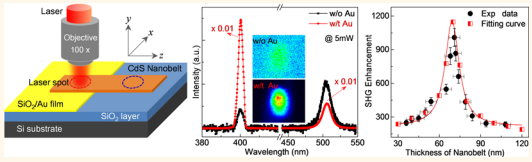

KEYWORDS: nonlinear optics · second-harmonic generation · CdS nanobelt · plasmonic nanocavity · Fabry–Pérot resonance · SHG enhancement · plasmons

Nonlinear optical properties play an important role in photonics, materials science, and bioimaging with functionalities such as frequency mixing, supercontinuum generation, and optical solitons.[1−4] Second-harmonic generation (SHG) is the lowest order frequency mixing nonlinear optical process where two photons create a single photon with half the incident wavelength.[5] This provides a convenient and practical means to obtain blue emission from a near-infrared laser and has found applications as nonlinear optical frequency converters, all-optical signal processors, and biosensors.[6−8] Specifically, achieving SHGs with nanowires/nanobelts (*e.g.*, in ZnO, GaN, GaP, and $KNbO_3$) would prove highly advantageous for nanoscale coherent light sources and integrated optical circuits.[9−12] Furthermore, light-emitting nanoscale probes have also been proposed as an ideal platform for single-molecule fluorescence imaging, single-molecule endoscopy, and *in vivo* cell imaging.[13−15] However, SHG is generally inefficient at such diminutive scales.[16−18] Many schemes to enhance SHG in nanostructures (*e.g.*, utilizing the Purcell effect,[19] structure tailoring,[17] interface strain,[20] and plasmonic effects[21]) have previously been proposed to overcome this severe limitation.[2,22] Among them, utilizing plasmonic effects is particularly compatible with the localization of highly concentrated local fields at resonance in the compact mode volumes of these nanostructures.[23−26]

Plasmonics, which involves the coupling between electromagnetic radiation and collective electronic oscillations (or surface plasmons) in metals, is also relevant for the manipulation of light at the nanoscale.[27−29] Plasmonic structures enhance the nonlinear effects in the following ways: (a) such nanostructures provide field enhancement near

* Address correspondence to Tzechien@ntu.edu.sg, Qihua@ntu.edu.sg.

Received for review December 17, 2014 and accepted April 23, 2015.

Published online April 23, 2015
10.1021/nn5072045

the metal–dielectric interface, associated with the excitation of either surface plasmon polaritons (SPPs) or localized surface plasmons (LSPs), or (b) the nonlinear change of the refractive index in either material can significantly modify plasmonic resonances and associated reflection, transmission, or absorption of light.[2] Presently, most works on enhancing nonlinear effects are either focused on the metal nanostructures (*e.g.*, nanoaperture silver film,[30] gold bowtie antenna,[31] non-centrosymmetric gold nanocup,[32] gold gratings,[33] and tapered plasmonic silver waveguide[34]) or focused on enhancing the nonlinear properties of semiconductors at the single nanoscale structure level (*e.g.*, SHG from single core–shell quantum dots,[35] ZnO nanowire,[36] $KNbO_3$ nanowire,[37] and $KTiOPO_4$[38,39]). Studies on enhancing the SHG from a single nanostructure using plasmonic effects are rarely reported. To the best of our knowledge, these studies include (a) the demonstration of large enhancement of SHG in $BaTiO_3$/Au core–shell structures utilizing the entire mode volume for an even-order nonlinear optical process by Pu *et al.*,[21] (b) the detection of a second-order optical response from a single sphere comprising a centrosymmetric material coated with a nonlinear material by Vidal *et al.*,[40] (c) the generation of high-efficiency second-harmonic responses from a single hybrid ZnO nanowire/Au plasmonic nano-oligomer by Gustavo *et al.*,[41] (d) enhanced nonlinear response of single GaAs nanowires by coupling to optical nanoantennas,[42] and (e) enhanced optical signal in the near-infrared spectral range by using a $KNbO_3$–Au core–shell structure.[43] More recently, enhanced second-harmonic generation from metal-integrated CdS semiconductor nanowires was reported by Agarwal *et al*. through the highly confined whispering gallery modes.[44] These related reports of SHG enhancements are summarized in the Supporting Information, as shown in Table S1. Some of the enhancement factors evaluated in the listed works are not average values, but the enhancement factor of the hot-spots. The actual enhancement value would be lower. Several works utilized electron beam methods to fabricate metal structures with high resolution. This would incur high costs or require some form of elaborate nanostructure synthesis/preparation. Our hybrid nonlinear media, low dielectric, and metal hybrid structures on the other hand are attractive not only for industrial applications for its low cost and facile preparation but also for fundamental studies.

In this work, we report on a straightforward approach to enhance the SHG from a single CdS nanobelt by 3 orders of magnitude using a simple yet versatile hybrid plasmonic configuration. Using detailed experimental studies and theoretical analysis, we validate that the SHG enhancement arises from the collective augmentation of the local field and reflection induced by both the plasmonic nanocavity and the Fabry–Pérot resonance effects with this hybrid semiconductor–plasmonic structure. Polarization-dependent SHG measurements allow us to distinguish the respective contributions of SH signals from the CdS nanobelt and the gold film. The SHG from the Au film can be clearly observed when the thickness of the gold film becomes comparable to its skin depth. Importantly, our work demonstrates a facile approach to overcome the limitations of generating efficient nonlinear optical effects in single mesoscopic, nanostructured, or layered semiconductor materials.

RESULTS AND DISCUSSION

CdS has a wurtzite crystal structure and belongs to the 6 mm crystal class. Although it is a non-centrosymmetric crystal and has a significant second-order nonlinear susceptibility with nonzero components d_{15} = 44.0 pm V^{-1}, d_{31} = 40.2 pm V^{-1}, and d_{33} = 77.9 pm V^{-1} at 800 nm,[45] their nanostructures still suffer from the limitations of efficient second-harmonic generation. Our hybrid plasmonic nanocavity structure comprises the single CdS nanobelt separated from the underlying gold film by a thin layer of SiO_2 (see Figure 1a). Hence, this forms a cavity that sustains the Fabry–Pérot modes in both the vertical and horizontal directions. As the cavity mode is confined in a subwavelength volume, large fields are established in both the CdS and SiO_2 layers under resonant excitation conditions. Figure 1b shows the electric field distributions in the semiconductor/dielectric/metal structure excited at its resonant wavelength, simulated using the finite-difference time domain (FDTD) method. Figure 1c is the corresponding cross-sectional electric field intensity profiles for the CdS nanobelt and SiO_2 layer. To allow precise comparison, we prepared a single CdS nanobelt to span across the two dissimilar substrates, with part of the CdS on the SiO_2/Au substrate and the other on the bare SiO_2 substrate (see Figure 1a). A mode-locked Ti:sapphire laser (wavelength 760–840 nm) delivering 120 fs pulses at a repetition rate of 76 MHz was used as the excitation laser source. The fundamental beam was focused by a 100× objective onto the semiconductor nanobelt with the spot size of ~1.0 μm in diameter (see Supporting Information Figure S1). The second-harmonic (SH) signal was collected by the same objective and detected by a spectrometer equipped with a thermoelectric-cooled silicon charge-coupled device (CCD) camera. A set of color filters was used to block the fundamental and other unwanted light. Figure 1d is a typical scanning electron microscope (SEM) image of a single CdS nanobelt (several micrometers in length and ~1.2 μm wide) lying partially on the SiO_2/Au and SiO_2 substrates. This configuration provides us with a means to obtain fair comparison of the SH signals from the same belt but on different substrates. Corresponding atomic force microscope (AFM) images were also obtained

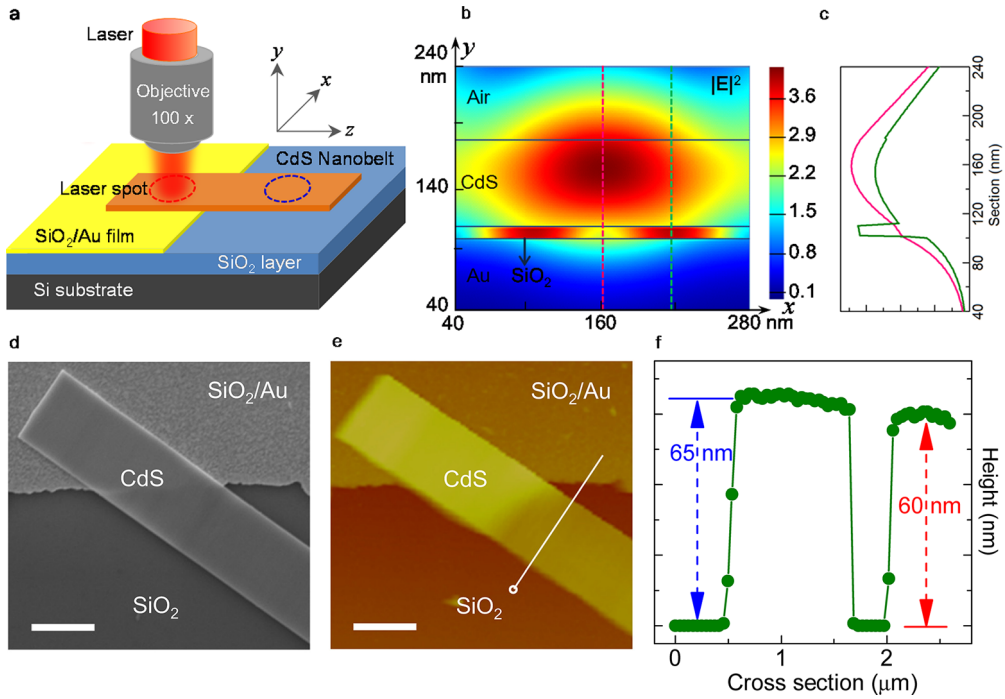

Figure 1. (a) Schematic of the SHG measurements on a single CdS nanobelt. To permit direct comparison of the SHG enhancement, part of the belt was on the SiO_2 layer and part of the belt was on the SiO_2/Au substrate. The red and blue dashed circle lines are the focused laser spot. (b) Electric field distribution (x, y) in the semiconductor/dielectric/metal structure excited with a focused laser spot. (c) Corresponding cross sectional intensity profiles of the structure shown in b indicated by the green and pink dashed lines. (d) SEM image of the single CdS nanobelt straddling the SiO_2/Au and SiO_2 regions, where the scale bar is 1 μm. (e) Corresponding AFM image of the nanobelt shown in d, where the scale bar is 1 μm. (f) Cross sectional profile showing the thickness of the CdS nanobelt (~65 nm) and Au film (~60 nm), extracted from the white line in e.

to determine the thickness of the CdS nanobelt and Au film. From the cross sectional profile (see Figure 1e and f), we determine the thicknesses of the CdS and Au to be 65 and 60 nm, respectively. In all subsequent experiments, all the thicknesses of CdS nanobelts were determined by the accompanying AFM measurements.

Figure 2a compares the second-harmonic emission spectra for the same single CdS nanobelt on the hybrid plasmonic structure with the Au film and on bare SiO_2 without the Au film. The fundamental excitation laser wavelength is 800 nm with a fixed power of 5 mW. At the frequency-doubled signal of the pump laser, a strong SH signal at 400 nm is measured. The relatively small peak located at 510 nm originates from the much weaker two-photon-induced photoluminescence (TPL) process since the photon energy of the pump laser (1.55 eV) is smaller than the band gap of CdS (~2.4 eV).[46,47] It is evident that the SH signal from the hybrid plasmonic structure is around 400 times larger than that from the bare SiO_2. Figure 2a (inset) shows the CCD images of the second-harmonic signal for these two regions of the same single CdS nanobelt on different substrates. The power-dependent SH signal exhibits quadratic input power dependence, confirming the second-order nature of the nonlinear process (see Figure 2b). A simple estimate of the efficiency of the measured SH generation light from the CdS nanobelt is $\sim 2 \times 10^{-6}$ % at a pumping power of 5 mW, where a single layer MoS_2 was used as the standard sample for calibration (see Supporting Information Figure S2).

To investigate the effect of the CdS nanobelt thickness on the SHG enhancement, we conducted a set of measurements on CdS nanobelts with different thicknesses. The SHG enhancement is defined as I_E/I_O, where I_E and I_O represent the integrated intensities of the SHG from CdS on the hybrid plasmonic structure and that on bare SiO_2, respectively. Figure 3a shows the enhancement of the SHG signal for a pump power of 5 mW at 800 nm from different CdS nanobelts with thickness ranging from 38 to 110 nm (black dots). When the thickness of the CdS nanobelts is around 70 nm, there exists a maximum enhancement of the SHG from the CdS/SiO_2/Au hybrid structure. On the basis of previous reports, two predominant effects, the plasmonic nanocavity effect and Fabry–Pérot cavity resonance, are thus proposed to account for this behavior.[33,48,49] As shown in Figure 1b, two strong electric fields are observed when excited using the 800 nm pump laser; one is located within the CdS nanobelt and the other is within the SiO_2 layer. Furthermore, a different reflection parameter at 400 nm should also be considered due to different reflectivities on Au/SiO_2 and on bare SiO_2 substrates. On the basis of the above discussion, we simulate the electric field

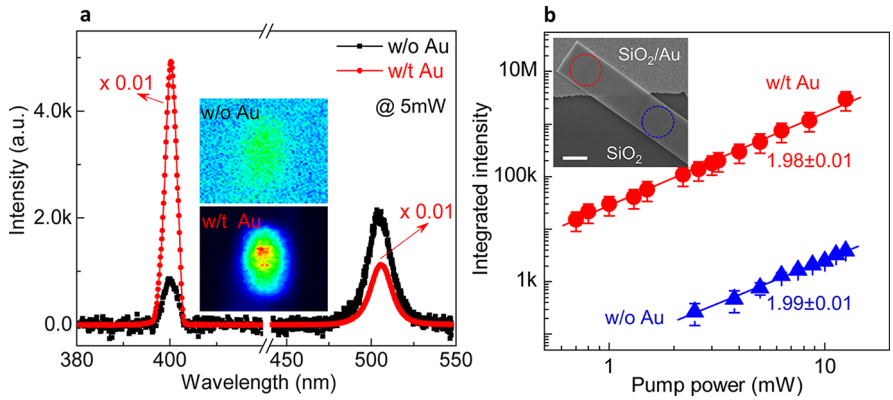

Figure 2. (a) Spectra of the second-harmonic (SH) signals from a single CdS nanobelt on SiO_2 (red circle in b, on SEM image) and on SiO_2/Au (blue circle in b, on SEM image). The excitation wavelength is 800 nm with a power of 5 mW, the peaks around 400 nm are the SH signal, and the peaks around 510 nm are two-photon emission of the CdS nanobelt. Note that the extremely large SH signal from the CdS nanobelt at the SiO_2/Au region has been scaled to be 100 times smaller. Inset shows the corresponding CCD images for these two regions of a single CdS nanobelt. (b) Measured SH intensity *versus* fundamental laser power on a log−log scale. The blue triangles represent the results for the CdS nanobelt on SiO_2, while the red dots are for the CdS nanobelt on SiO_2/Au. The solid lines show a linear fit with a slope of approximately 2.

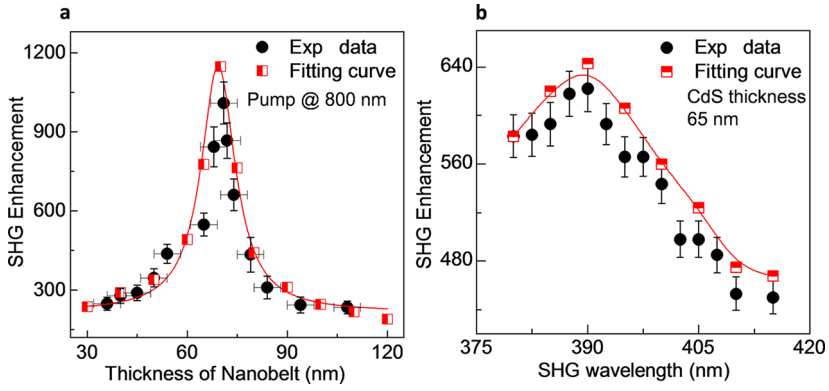

Figure 3. (a) SHG enhancement as a function of the CdS nanobelt thickness. The black dots are the experimental data, and the red line is the fitting curve. The fitting data points are calculated from the simulation results using FDTD. (b) SHG enhancement as a function of the laser excitation wavelength. The enhancement is defined as the ratio between the integrated SH signal from CdS on SiO_2/Au and that from CdS on SiO_2. The black dot is the experimental data, and the red line is the fitting curve. The fitting data points are calculated from the simulation results using FDTD.

distribution inside these two systems (a CdS nanobelt with and without plasmonic cavity) at 800 nm and utilize different reflection parameters at 400 nm using the FDTD method (see Supporting Information Figure S3). In our simulations, we calculated the near-field distribution of excitation light (λ) E_{ex}^2 and far-field distribution of out-coupling SHG ($\lambda/2$) E_{SHG}^2 using FDTD. Essentially, the collected SHG signal is proportional to E_{ex}^4 and E_{SHG}^2. Only by taking into account both plasmonic and Fabry−Pérot effects can the experimental data be well explained, as shown in Figure S4. The underlying physical mechanism for near-field enhancement is the plasmonic effect, while the thickness-dependent far-field intensity is due to the Fabry−Pérot effect in the light propagation direction induced by the refractive index variation at the two surfaces of the CdS nanobelt. Given that it is well known that the factor of enhancement on the total SHG power shows a fourth-order dependence on the electric fields,[21,50] the enhancement factor (Γ_{SHG}) of the total SHG emission power is then calculated using the following equation: $\Gamma_{SHG} = I_{Au}/I_{SiO2} = [(E_{CdS}/E_0)^4 + (E_{SiO2}/E_0)^4]R_F$, where I_{Au} and I_{SiO2} are the SHG intensity from the plasmonic structure and bare SiO_2, respectively; E_{CdS} and E_{SiO2} are the electric field intensities inside the CdS and SiO_2 layer, respectively, with the plasmonic structure; E_0 is the electric field without the plasmonic structure inside the CdS/SiO_2 layer; and R_F is the reflection enhancement with and without the Au film at $\lambda/2$ wavelength. The electric field distributions with and without the plasmonic structure for a CdS nanobelt of thickness 60 nm are shown in Figure S3a and b. The reflection enhancement for different wavelengths is shown in Figure S3c. The simulation data are also plotted in Figure 3a (red line; see Supporting Information Table S2 for more details), which are well fitted with the experimental data. To further study the spectral dependence of the enhancement and gain deeper insight into the behavior of the hybrid plasmonic structure, the fundamental laser wavelength is

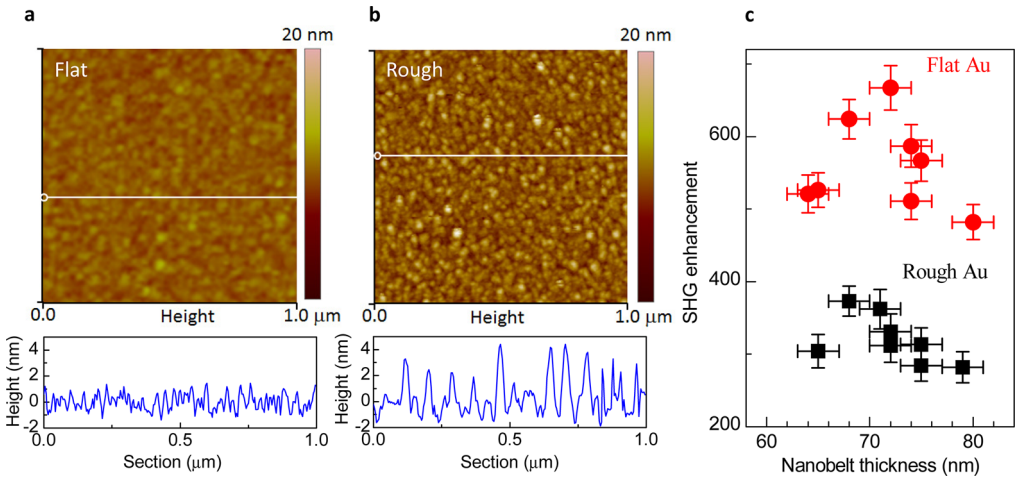

Figure 4. AFM images of relatively smooth (0.6 ± 0.1 nm) (a) and rough (1.9 ± 0.3 nm) (b) Au films with a scan area of 1 μm × 1 μm. The cross-sectional profiles below the images show the roughness of the measured Au film. (c) SHG enhancement for CdS nanobelts with different thicknesses on flat (red dots) and rough (black dots) Au films. Similarly, the enhancement is also defined as the ratio between the integrated SH signal from CdS on SiO_2/Au *versus* that from CdS on SiO_2.

tuned while keeping the laser beam on the same spot. Wavelength-dependent measurements of the SH enhancement are shown in Figure 3b, where an enhancement peak of SHG at around 390 nm is observed. The simulation data fit the experimental results well (red line in Figure 3b; see Supporting Information Table S3 for more details). From both the thickness- and wavelength-dependent SHG enhancements, the good correspondence between the experimental data and the simulation results strongly supports our proposed cooperative mechanisms (both plasmonic nanocavity and Fabry−Pérot resonance effects) for the observed phenomena. The plasmonic effect, which is based on the collective oscillation of free electrons at the metal−dielectric interface, provides a useful approach to tailor the light−matter interactions at the nanoscale. By confining the optical energy at the subwavelength limit, the cross sections of various linear and nonlinear optical processes can thus be enhanced. On the other hand, the Fabry−Pérot cavity resonance, which is related to the thickness of the CdS nanobelt, affects the SHG emission by improving the in- and outcoupling efficiency of the excitation light source and the SH signal.

From previous literature, the plasmonic nanocavity has been used to enhance the carrier densities[47,51] and various nonlinear optical phenomena.[44,52] In our case, as the cavity mode is predominantly confined within the SiO_2 and CdS layers, large fields are established in both the dielectric and semiconductor under resonant excitations. Plamonic hybrid structures are designed to enhance the nonlinear effects by providing field enhancement near the metal−dielectric interface in the form of surface polariton plasmons. An increased effective nonlinear optical response can be achieved through plasmonic effects arising from coherent oscillations of conduction electrons near the surface of noble-metal structures. In these processes, the surface roughness of the Au film is expected to play an important role toward establishing a strong electric field in the SiO_2 layer. In the following experiments, Au films with different roughness are fabricated to study their dependence on the SHG enhancement. Figure 4a and b show the surface roughness of two kinds of Au films with root-mean-square (RMS) roughness of 0.6 ± 0.1 nm and 1.9 ± 0.3 nm, respectively. After that, one layer of SiO_2 with a thickness of ~10 nm is deposited onto the surface of the Au film. Using these two substrates, we compare the SHG enhancement from the CdS nanobelts. Batches of CdS nanobelts with different thicknesses were measured, and the corresponding enhancements are plotted in Figure 4c. From the comparison, it is evident that the relatively rougher Au films reduce the enhancement due to the plasmonic losses and the weaker electric field within the SiO_2 layer. This roughness-dependent behavior shows that a high-quality gold film is paramount to generating strong electric fields in such metal/dielectric/semiconductor plasmonic cavity structures. Our findings concur with that of Lu *et al.*, who had previously demonstrated that smooth metallic films are crucial for reducing the plasmonic loss and forming a strong electric field inside the plasmonic cavity.[53]

To gain deeper insights into the dependence of the SHG on the crystal orientations of the CdS nanobelt, polarization-dependent characteristics of the measured SHG signals from CdS on a SiO_2/Au substrate were also systematically studied. The configuration of the polarization-dependent measurement is shown in Figure 5a (for the detailed experimental setup, see Supporting Information Figure S5). Here, e and e' represent the laboratory and crystalline coordinates, respectively. The pump laser polarization can be tuned from $\theta = 0°$ to 360°, where θ is the angle between the

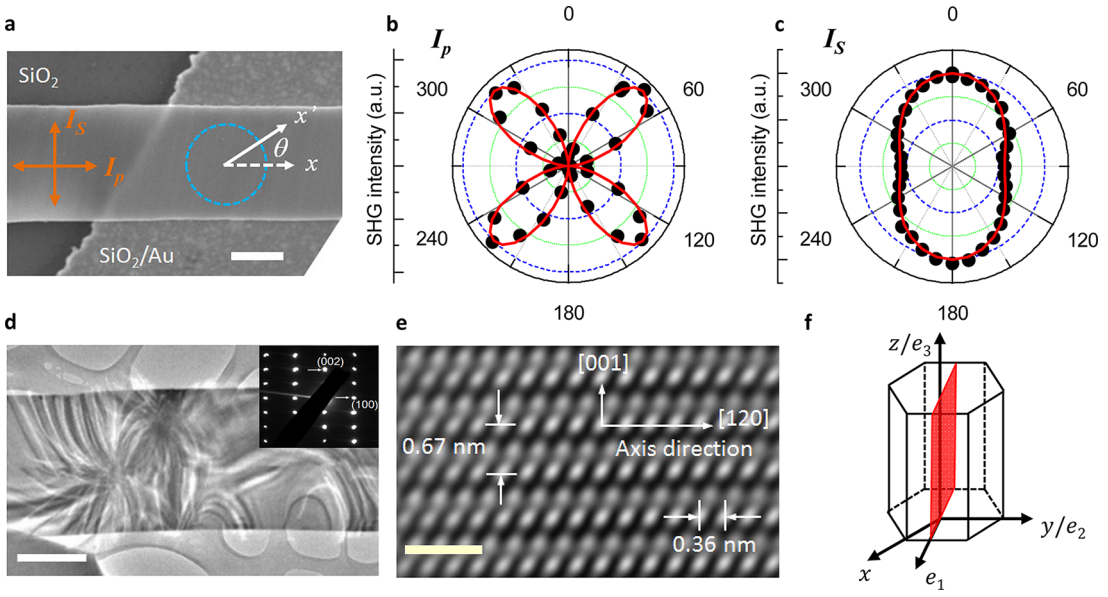

Figure 5. (a) Configuration of the polarization-dependent SHG intensity. x and x' represent the laboratory and crystalline coordinates, respectively. The pump laser polarization is from $\theta = 0°$ to 360°, where θ is the angle between the laboratory and crystalline coordinates. The parallel and perpendicular components of the SHG intensity are defined as I_P and I_S. The scale is 1 μm. (b and(c) SHG intensity of the I_P and I_S components as a function of θ. The red solid line indicates the fitting curves using eqs 1 and 2. (d) TEM image of a typical CdS nanobelt. Inset shows the corresponding electron diffraction pattern; the scale bar is 1 μm. (e) High-resolution TEM image from d. The crystal growth direction is along the [120] direction. The scale bar is 1 nm. (f) Structural model for the CdS nanobelt. (x, y, z) represent the crystal coordinates, (e_1, e_2, e_3) represent the laboratory coordinates, and the red parallelogram is the CdS nanobelt.

laboratory and crystalline coordinates, which is controlled using a $\lambda/2$ waveplate polarizer. The system was calibrated to remove any possible artifacts from the substrate (see Supporting Information Figure S6). The parallel and perpendicular components of the SHG intensity, defined as I_P and I_S, respectively, are distinguished by means of a polarizer in front of the monochromator. Figure 5b and c present the parallel (I_P) and perpendicular (I_S) components (the black dots) of the total SHG intensity from the CdS on SiO_2/Au substrates, as a function of the pump laser polarization angle (θ). To permit theoretical analysis of the polarization-dependent SHG pattern, the crystal structure of the CdS nanobelt and the configuration of the excitation/collection optics need to be clearly defined. Figure 5d shows a typical TEM image of a single CdS nanobelt, and transmission electron diffraction (TED) patterns confirm that the CdS nanobelts are single crystalline. The corresponding high-resolution TEM image is given in Figure 5e. A universal growth direction (along the hexagonal [120] direction) is evidenced by the Fourier transform (inset of Figure 5d) taken from the high-resolution image (see Figure 5e). The structural model for the CdS nanobelt is shown in Figure 5f, where (x, y, z) represent the crystal coordinates, (e_1, e_2, e_3) represent the laboratory coordinates, and the red parallelogram is the CdS nanobelt. The theoretical calculation results based on the structural model is further carried out to support our experimental data. The intensities of the parallel and perpendicular SHG components (I_P and I_S) can be written as the following two expressions (see Supporting Information and Figure S7 for the derivation):

$$I_P = 4k_1\varepsilon_0{}^2E_0{}^4A^2(\sin^2 2\theta) \quad (1)$$

$$I_S = k_2\varepsilon_0{}^2E_0{}^4\left(\frac{5}{3}B\sin^2\theta + C\cos^2\theta\right)^2 \quad (2)$$

where k_1, k_2, A, B, and C are parameters related to the materials.[54,55] The solid red lines in Figure 5b and c are theoretical fittings using eqs 1 and 2, respectively, indicating that the anisotropy of the SHG originates from the intrinsic symmetry of the CdS crystal lattice.

Lastly, we extend these polarization-dependent measurements to examine the contributions from the Au surface to the SHG signal. Au films of different thickness (but with comparable surface roughness ~0.6 nm) were used for comparison, and the polarization-dependent SHG signals (I_S) are used to distinguish this point (I_P was not used here to distinguish the contribution from the Au film and CdS nanobelt due to the Au film and CdS nanobelt sharing the same expression of I_P α $\sin^2 2\theta$). It should be noted that, for the SHG from the semiconductor and metal film, the signal from the CdS nanobelt is overwhelmingly stronger than that from the gold surface (we measured almost no SHG signal from the bare Au film in our reflection configuration).[44,48] Therefore, thinner CdS nanobelts (40 ± 5 nm in thickness) were employed here to elucidate the SHG signal from the gold surface. It should also be noted that the thickness of the gold

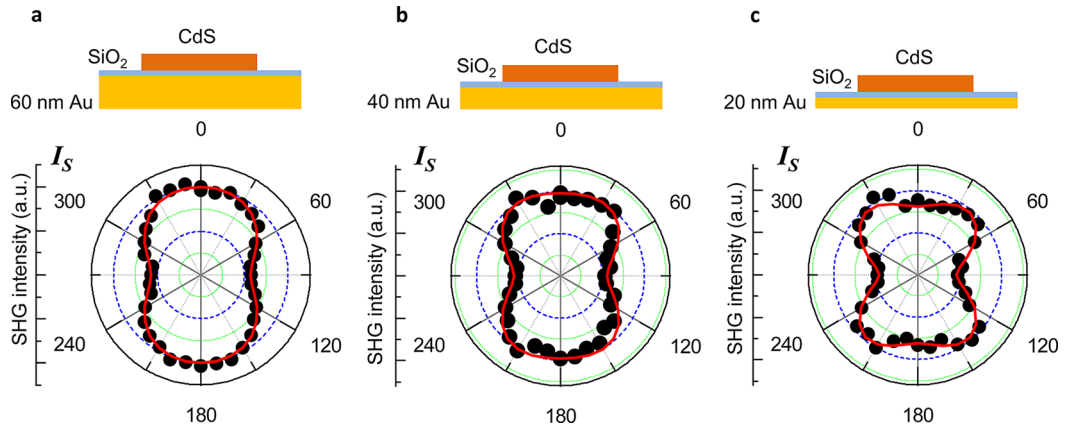

Figure 6. SHG intensity of the I_S component with different Au film thickness: (a) 60 nm, (b) 40 nm, and (c) 20 nm. The pump laser wavelength is 800 nm with a pump power of 3 mW. The thickness of the CdS nanobelt used here was around 40 ± 10 nm. The red sold lines are fitting curves considering the contribution of SHG signals from both the CdS nanobelt and Au film.

film cannot be thinner than 20 nm because of the formation of gold islands when thermally evaporating gold on SiO_2/Si. These gold islands will lift the momentum conservation and result in nondirectional emission, yielding a totally different situation from our discussion. Therefore, the Au films used in our experiment ranged from around 20 to 60 nm. The perpendicular SHG component for 60 nm thick Au presented in Figure 6a shows similar patterns to those in Figure 5c. This suggests that the SH signal from the CdS nanobelt should still dominate the measured result. Theoretically, we can superpose the SH signal both from the CdS nanobelt and the Au film to fit the experimental data; I_S components from the CdS nanobelt and Au film can be expressed as $(0.75 \sin^2\theta + \cos^2\theta)^2$ and $\sin^2 2\theta$, respectively.[56] From the fitting curve in Figure 6a, the contributions of the SH signal from the Au surface and CdS nanobelt were 6% and 94%, respectively. By decreasing the thickness of the Au film from 60 nm to 40 and 20 nm, as shown in Figure 6b and c, the contribution to the SH signal from the Au surface increases from 15% to 28%. This thickness-dependent behavior can be understood in terms of the skin depth of the Au film. When the Au thickness becomes comparable to the skin depth of Au (*i.e.*, ~30 nm),[57] the evanescent field could also interact with the bottom Au/SiO_2 interface. The enhanced fields (from 800 nm) in the Au film can be viewed as an interference effect: the incident 800 nm pump will be reflected from both the top SiO_2/Au interface and the bottom Au/SiO_2 interface. When both 800 nm pump waves are nearly out of phase (dependent on the Au layer thickness), less reflection from these interfaces occurs, leaving behind more energy in the metal film for SHG generation. Hence an enhanced SHG is detected.

The interfaces and surfaces are always crucial in determining the SH signals. In semiconductor CdS nanobelts, the SHG originates from the surface (as the symmetry is broken by the presence of interface) and the bulk (due to the inherent non-centrosymmetry of CdS). However, based on our present excitation geometry, the surface contribution to the SHG is expected to be small. This is validated by our polarization-dependent SHG, which shows good agreement with the SHG arising from the crystal structure (*i.e.*, bulk contributions). However, for the Au film, SHG is not possible in centrosymmetric materials, but may be observed at the surface where the symmetry is broken.

Although the lateral size of a nanobelt is also relatively large, its modal confinement is not as high as that of a nanowire. However, its large planar surface in contact with the underlying metal allows for more effective interaction and higher modal coupling efficiency with the SPP modes. A larger interaction area would strengthen the signal, thus resulting in a hybrid plasmonic cavity with much higher quality factors. This is similar to the approach used in realizing a room-temperature low-loss plasmonic laser.[58] Although nanowires with hexagonal or triangular cross sections would allow for larger interaction areas compared to circular nanowires, their protruding nanowire cross sections would still be unsuitable for integration with planar layers. Nanobelts, on the hand, would be more amenable for planar integration.

CONCLUSIONS

In summary, we report on a straightforward approach to enhance the SHG from a single CdS nanobelt through a facile, yet versatile hybrid plasmonic structure. A maximum enhancement of SHG (>1000) is observed, when the thickness of CdS nanobelts is ~70 nm at a wavelength of ~780 nm, as a result of the cooperative enhancement of the local field and reflection induced by both the plasmonic nanocavity and Fabry–Pérot resonance effects. We validate these findings using detailed experimental studies and theoretical analysis. Polarization-dependent SHG measurements were employed to determine and distinguish the contributions from the CdS nanobelt and gold film. When the thickness of the gold film becomes

comparable to its skin depth, an interference effect occurs and SHG from gold can be clearly observed. Importantly, our findings present an efficient and reproducible method for investigating and tuning the nonlinear optical properties for single mesoscopic, nanostructured, or layered semiconductor materials.

METHODS

The CdS nanobelts were synthesized in a home-built, vapor-transport chemical vapor-deposition system. Synthesis and characterization details have been published elsewhere. The as-prepared CdS nanobelts were dispersed in ethanol by sonication and then drop-casted onto the as-prepared substrates, which have arrays of Au pads covered with different thicknesses of SiO_2. The arrays of Au pads were fabricated with electron beam lithography solely for the purpose of permitting direct comparison of the SHG enhancement with part of the belt on the SiO_2 layer and part of the belt was on the SiO_2/Au substrate. After drying the sample in the air, individual CdS nanobelts overlapping both the Au pads and bare SiO_2/silicon parts could be found by optical microscopy.

Second-harmonic generation measurements were performed by using excitation pulses from a Coherent Mira 900 fs laser system with an output wavelength from 760 to 840 nm and a repetition rate of 76 MHz. The SH signal was dispersed by a 300 mm monochromator with 150 g mm^{-1} grating and collected by a thermoelectrically cooled CCD. The polarization-dependent SHG measurement setup can be seen in Supporting Information Figure S5. Full-field electromagnetic wave calculations were performed using Lumerical, a commercial finite-difference time-domain simulation software package.[59,60] A two-dimensional simulation scenario was used, as the CdS NW direction can be treated to be infinitely long. An antisymmetric boundary condition was set along the polarization of electromagnetic waves (x axis); perfectly matched layers were used along the propagation of electromagnetic waves (y axis). Electric and magnetic fields are detected using frequency profile monitors. Dielectric constants of CdS, SiO_2, Si, and Au are extracted from previous reports.[26,61]

Conflict of Interest: The authors declare no competing financial interest.

Acknowledgment. T.C.S. acknowledges the support from the following research grants: NTU start-up grants (M4080514); SPMS Collaborative Research Award (M4080536); Ministry of Education (MOE) Academic Research Fund (AcRF) Tier 2 grants MOE2011-T2-2-051 and MOE2013-T2-1-081. X.F.L. and T.C.S. also acknowledge the financial support by the Singapore National Research Foundation through the Competitive Research Programme under Project No. NRF-CRP5-2009-04 and the Singapore-Berkeley Research Initiative for Sustainable Energy (SinBerRISE) CREATE Programme. Q.X. acknowledges the support of this work from the Singapore National Research Foundation through an NRF fellowship grant (NRF-RF2009-06) and a Competitive Research Program grant (NRF-CRP-6-2010-2), Ministry of Education AcRF Tier 2 grant (MOE2011-T2-2-051), a MOE Tier1 grant (MOE2013-T1-002-232) and start-up grant support (M58113004) from Nanyang Technological University.

Supporting Information Available: Supporting Information for the experimental results is available free of charge on the ACS Publications website at DOI: 10.1021/nn5072045.

REFERENCES AND NOTES

1. Berger, V. Nonlinear Photonic Crystals. *Phys. Rev. Lett.* **1998**, *81*, 4136–4139.
2. Kauranen, M.; Zayats, A. V. Nonlinear Plasmonics. *Nat. Photonics* **2012**, *6*, 737–748.
3. Moss, D. J.; Morandotti, R.; Gaeta, A. L.; Lipson, M. New Cmos-Compatible Platforms Based on Silicon Nitride and Hydex for Nonlinear Optics. *Nat. Photonics* **2013**, *7*, 597–607.
4. Harutyunyan, H.; Palomba, S.; Renger, J.; Quidant, R.; Novotny, L. Nonlinear Dark-Field Microscopy. *Nano Lett.* **2010**, *10*, 5076–5079.
5. Franken, P. A.; Hill, A. E.; Peters, C. W.; Weinreich, G. Generation of Optical Harmonics. *Phys. Rev. Lett.* **1961**, *7*, 118–119.
6. Danckwerts, M.; Novotny, L. Optical Frequency Mixing at Coupled Gold Nanoparticles. *Phys. Rev. Lett.* **2007**, *98*, 026104.
7. Press, D.; De Greve, K.; McMahon, P. L.; Ladd, T. D.; Friess, B.; Schneider, C.; Kamp, M.; Hofling, S.; Forchel, A.; Yamamoto, Y. Ultrafast Optical Spin Echo in a Single Quantum Dot. *Nat. Photonics* **2010**, *4*, 367–370.
8. Brolo, A. G. Plasmonics for Future Biosensors. *Nat. Photonics* **2012**, *6*, 709–713.
9. Johnson, J. C.; Yan, H.; Schaller, R. D.; Petersen, P. B.; Yang, P.; Saykally, R. J. Near-Field Imaging of Nonlinear Optical Mixing in Single Zinc Oxide Nanowires. *Nano Lett.* **2002**, *2*, 279–283.
10. Long, J. P.; Simpkins, B. S.; Rowenhorst, D. J.; Pehrsson, P. E. Far-Field Imaging of Optical Second-Harmonic Generation in Single GaN Nanowires. *Nano Lett.* **2007**, *7*, 831–836.
11. Dutto, F.; Raillon, C.; Schenk, K.; Radenovic, A. Nonlinear Optical Response in Single Alkaline Niobate Nanowires. *Nano Lett.* **2011**, *11*, 2517–2521.
12. Sanatinia, R.; Anand, S.; Swillo, M. Modal Engineering of Second-Harmonic Generation in Single Gap Nanopillars. *Nano Lett.* **2014**, *14*, 5376–5381.
13. Yang, P. D.; Yan, R. X.; Fardy, M. Semiconductor Nanowire: What's Next? *Nano Lett.* **2010**, *10*, 1529–1536.
14. Xie, C.; Hanson, L.; Cui, Y.; Cui, B. X. Vertical Nanopillars for Highly Localized Fluorescence Imaging. *Proc. Natl. Acad. Sci. U.S.A.* **2011**, *108*, 3894–3899.
15. Pantazis, P.; Maloney, J.; Wu, D.; Fraser, S. E. Second Harmonic Generating (SHG) Nanoprobes for *in Vivo* Imaging. *Proc. Natl. Acad. Sci. U.S.A.* **2010**, *107*, 14535–14540.
16. Sanatinia, R.; Swillo, M.; Anand, S. Surface Second-Harmonic Generation from Vertical Gap Nanopillars. *Nano Lett.* **2012**, *12*, 820–826.
17. Dutto, F.; Heiss, M.; Lovera, A.; López-Sánchez, O.; Fontcuberta i Morral, A.; Radenovic, A. Enhancement of Second Harmonic Signal in Nanofabricated Cones. *Nano Lett.* **2013**, *13*, 6048–6054.
18. Liu, W.; Wang, K.; Liu, Z.; Shen, G.; Lu, P. Laterally Emitted Surface Second Harmonic Generation in a Single ZnTe Nanowire. *Nano Lett.* **2013**, *13*, 4224–4229.
19. Bermel, P.; Rodriguez, A.; Joannopoulos, J. D.; Soljačić, M. Tailoring Optical Nonlinearities *via* the Purcell Effect. *Phys. Rev. Lett.* **2007**, *99*, 053601.
20. Cazzanelli, M.; Bianco, F.; Borga, E.; Pucker, G.; Ghulinyan, M.; Degoli, E.; Luppi, E.; Véniard, V.; Ossicini, S.; Modotto, D.; *et al.* Second-Harmonic Generation in Silicon Waveguides Strained by Silicon Nitride. *Nat. Mater.* **2012**, *11*, 148–154.
21. Pu, Y.; Grange, R.; Hsieh, C.-L.; Psaltis, D. Nonlinear Optical Properties of Core-Shell Nanocavities for Enhanced Second-Harmonic Generation. *Phys. Rev. Lett.* **2010**, *104*, 207402.
22. Hasan, S. B.; Lederer, F.; Rockstuhl, C. Nonlinear Plasmonic Antennas. *Mater. Today* **2014**, *17*, 478–485.
23. Halas, N. J. Plasmonics: An Emerging Field Fostered by Nano Letters. *Nano Lett.* **2010**, *10*, 3816–3822.
24. Bouhelier, A.; Beversluis, M.; Hartschuh, A.; Novotny, L. Near-Field Second-Harmonic Generation Induced by Local Field Enhancement. *Phys. Rev. Lett.* **2003**, *90*, 013903.
25. Chen, K.; Durak, C.; Heflin, J. R.; Robinson, H. D. Plasmon-Enhanced Second-Harmonic Generation from Ionic Self-Assembled Multilayer Films. *Nano Lett.* **2006**, *7*, 254–258.

26. Liu, X.; Zhang, Q.; Yip, J. N.; Xiong, Q.; Sum, T. C. Wavelength Tunable Single Nanowire Lasers Based on Surface Plasmon Polariton Enhanced Burstein–Moss Effect. *Nano Lett.* **2013**, *13*, 5336–5343.
27. Schuller, J. A.; Barnard, E. S.; Cai, W.; Jun, Y. C.; White, J. S.; Brongersma, M. L. Plasmonics for Extreme Light Concentration and Manipulation. *Nat. Mater.* **2010**, *9*, 193–204.
28. Gramotnev, D. K.; Bozhevolnyi, S. I. Plasmonics beyond the Diffraction Limit. *Nat. Photonics* **2010**, *4*, 83–91.
29. Maier, S. A.; Atwater, H. A. Plasmonics: Localization and Guiding of Electromagnetic Energy in Metal/Dielectric Structures. *J. Appl. Phys.* **2005**, *98*, 011101.
30. Nahata, A.; Linke, R. A.; Ishi, T.; Ohashi, K. Enhanced Nonlinear Optical Conversion from a Periodically Nanostructured Metal Film. *Opt. Lett.* **2003**, *28*, 423–425.
31. Hanke, T.; Cesar, J.; Knittel, V.; Trügler, A.; Hohenester, U.; Leitenstorfer, A.; Bratschitsch, R. Tailoring Spatiotemporal Light Confinement in Single Plasmonic Nanoantennas. *Nano Lett.* **2012**, *12*, 992–996.
32. Zhang, Y.; Grady, N. K.; Ayala-Orozco, C.; Halas, N. J. Three-Dimensional Nanostructures as Highly Efficient Generators of Second Harmonic Light. *Nano Lett.* **2011**, *11*, 5519–5523.
33. Genevet, P.; Tetienne, J.-P.; Gatzogiannis, E.; Blanchard, R.; Kats, M. A.; Scully, M. O.; Capasso, F. Large Enhancement of Nonlinear Optical Phenomena by Plasmonic Nanocavity Gratings. *Nano Lett.* **2010**, *10*, 4880–4883.
34. Park, I.-Y.; Kim, S.; Choi, J.; Lee, D.-H.; Kim, Y.-J.; Kling, M. F.; Stockman, M. I.; Kim, S.-W. Plasmonic Generation of Ultrashort Extreme-Ultraviolet Light Pulses. *Nat. Photonics* **2011**, *5*, 677–681.
35. Zielinski, M.; Oron, D.; Chauvat, D.; Zyss, J. Second-Harmonic Generation from a Single Core/Shell Quantum Dot. *Small* **2009**, *5*, 2835–2840.
36. Johnson, J. C.; Knutsen, K. P.; Yan, H.; Law, M.; Zhang, Y.; Yang, P.; Saykally, R. J. Ultrafast Carrier Dynamics in Single Zno Nanowire and Nanoribbon Lasers. *Nano Lett.* **2003**, *4*, 197–204.
37. Nakayama, Y.; Pauzauskie, P. J.; Radenovic, A.; Onorato, R. M.; Saykally, R. J.; Liphardt, J.; Yang, P. D. Tunable Nanowire Nonlinear Optical Probe. *Nature* **2007**, *447*, 1098–U8.
38. Le Xuan, L.; Zhou, C.; Slablab, A.; Chauvat, D.; Tard, C.; Perruchas, S.; Gacoin, T.; Villeval, P.; Roch, J. F. Photostable Second-Harmonic Generation from a Single $KTiOPO_4$ Nanocrystal for Nonlinear Microscopy. *Small* **2008**, *4*, 1332–1336.
39. Zielinski, M.; Winter, S.; Kolkowski, R.; Nogues, C.; Oron, D.; Zyss, J.; Chauvat, D. Nanoengineering the Second Order Susceptibility in Semiconductor Quantum Dot Heterostructures. *Opt. Express* **2011**, *19*, 6657–6670.
40. Vidal, X.; Fedyanin, A.; Molinos-Gómez, A.; Rao, S.; Martorell, J.; Petrov, D. Nonlinear Optical Response from Single Spheres Coated by a Nonlinear Monolayer. *Opt. Lett.* **2008**, *33*, 699–701.
41. Grinblat, G.; Rahmani, M.; Cortés, E.; Caldarola, M.; Comedi, D.; Maier, S. A.; Bragas, A. V. High-Efficiency Second Harmonic Generation from a Single Hybrid ZnO Nanowire/Au Plasmonic Nano-Oligomer. *Nano Lett.* **2014**, 6660–6665.
42. Casadei, A.; Pecora, E. F.; Trevino, J.; Forestiere, C.; Rüffer, D.; Russo-Averchi, E.; Matteini, F.; Tutuncuoglu, G.; Heiss, M.; Fontcuberta i Morral, A.; *et al.* Photonic–Plasmonic Coupling of GaAs Single Nanowires to Optical Nanoantennas. *Nano Lett.* **2014**, *14*, 2271–2278.
43. Richter, J.; Steinbruck, A.; Zilk, M.; Sergeyev, A.; Pertsch, T.; Tunnermann, A.; Grange, R. Core-Shell Potassium Niobate Nanowires for Enhanced Nonlinear Optical Effects. *Nanoscale* **2014**, *6*, 5200–5207.
44. Ren, M.-L.; Liu, W.; Aspetti, C. O.; Sun, L.; Agarwal, R. Enhanced Second-Harmonic Generation from Metal-Integrated Semiconductor Nanowires *via* Highly Confined Whispering Gallery Modes. *Nat. Commun.* **2014**, *5*, 5432.
45. Nirmal, M.; Dabbousi, B. O.; Bawendi, M. G.; Macklin, J. J.; Trautman, J. K.; Harris, T. D.; Brus, L. E. Fluorescence Intermittency in Single Cadmium Selenide Nanocrystals. *Nature* **1996**, *383*, 802–804.
46. Liu, X.; Zhang, Q.; Xing, G.; Xiong, Q.; Sum, T. C. Size-Dependent Exciton Recombination Dynamics in Single CdS Nanowires beyond the Quantum Confinement Regime. *J. Phys. Chem. C* **2013**, *117*, 10716–10722.
47. Liu, X.; Zhang, Q.; Xiong, Q.; Sum, T. C. Tailoring the Lasing Modes in Semiconductor Nanowire Cavities Using Intrinsic Self-Absorption. *Nano Lett.* **2013**, *13*, 1080–1085.
48. Renger, J.; Quidant, R.; Novotny, L. Enhanced Nonlinear Response from Metal Surfaces. *Opt. Express* **2011**, *19*, 1777–1785.
49. Thyagarajan, K.; Rivier, S.; Lovera, A.; Martin, O. J. F. Enhanced Second-Harmonic Generation from Double Resonant Plasmonic Antennae. *Opt. Express* **2012**, *20*, 12860–12865.
50. Dadap, J. I.; Shan, J.; Eisenthal, K. B.; Heinz, T. F. Second-Harmonic Rayleigh Scattering from a Sphere of Centrosymmetric Material. *Phys. Rev. Lett.* **1999**, *83*, 4045–4048.
51. Luther, J. M.; Jain, P. K.; Ewers, T.; Alivisatos, A. P. Localized Surface Plasmon Resonances Arising from Free Carriers in Doped Quantum Dots. *Nat. Mater.* **2011**, *10*, 361–366.
52. Ding, W.; Zhou, L.; Chou, S. Y. Enhancement and Electric Charge-Assisted Tuning of Nonlinear Light Generation in Bipolar Plasmonics. *Nano Lett.* **2014**, *14*, 2822–2830.
53. Lu, Y. J.; Kim, J.; Chen, H. Y.; Wu, C. H.; Dabidian, N.; Sanders, C. E.; Wang, C. Y.; Lu, M. Y.; Li, B. H.; Qiu, X. G.; *et al.* Plasmonic Nanolaser Using Epitaxially Grown Silver Film. *Science* **2012**, *337*, 450–453.
54. Shoji, I.; Kondo, T.; Kitamoto, A.; Shirane, M.; Ito, R. Absolute Scale of Second-Order Nonlinear-Optical Coefficients. *J. Opt. Soc. Am. B* **1997**, *14*, 2268–2294.
55. Boyd, R. W. *Nonlinear Opt.*, 3rd ed; Academic Press: Burlington, MA, 2008.
56. Butet, J.; Duboisset, J.; Bachelier, G.; Russier-Antoine, I.; Benichou, E.; Jonin, C.; Brevet, P.-F. Optical Second Harmonic Generation of Single Metallic Nanoparticles Embedded in a Homogeneous Medium. *Nano Lett.* **2010**, *10*, 1717–1721.
57. Manke, K. J.; Maznev, A. A.; Klieber, C.; Shalagatskyi, V.; Temnov, V. V.; Makarov, D.; Baek, S. H.; Eom, C. B.; Nelson, K. A. Measurement of Shorter-Than-Skin-Depth Acoustic Pulses in a Metal Film *via* Transient Reflectivity. *Appl. Phys. Lett.* **2013**, *103*, 173104.
58. Zhang, Q.; Li, G.; Liu, X.; Qian, F.; Li, Y.; Sum, T. C.; Lieber, C. M.; Xiong, Q. A Room Temperature Low-Threshold Ultraviolet Plasmonic Nanolaser. *Nat. Commun.* **2014**, *5*, 4953.
59. Liu, X.; Wu, B.; Zhang, Q.; Yip, J. N.; Yu, G.; Xiong, Q.; Mathews, N.; Sum, T. C. Elucidating the Localized Plasmonic Enhancement Effects from a Single Ag Nanowire in Organic Solar Cells. *ACS Nano* **2014**, *8*, 10101–10110.
60. Liu, X.; Ha, S. T.; Zhang, Q.; de la Mata, M.; Magen, C.; Arbiol, J.; Sum, T. C.; Xiong, Q. Whispering Gallery Mode Lasing from Hexagonal Shaped Layered Lead Iodide Crystals. *ACS Nano* **2015**, *9*, 687–695.
61. Buso, D.; Nicoletti, E.; Li, J.; Gu, M. Engineering the Refractive Index of Three-Dimensional Photonic Crystals through Multilayer Deposition of CdS Films. *Opt. Express* **2010**, *18*, 1033–1040.